Properties of dust particles in comets from photometric and polarimetric observations of 67P

Edith Hadamcik, Anny Chantal Levasseur-Regourd, Dean C. Hines, Asoke K. Sen, Jérémie Lasue, Jean-Baptiste Renard

Monthly Notices
of the
ROYAL ASTRONOMICAL SOCIETY

MNRAS **462,** S507–S515 (2017)
Advance Access publication 2016 December 17

doi:10.1093/mnras/stx030

Properties of dust particles in comets from photometric and polarimetric observations of 67P

E. Hadamcik,[1★] A.C. Levasseur-Regourd,[2★] D.C. Hines,[3] A.K. Sen,[4] J. Lasue[5] and J.-B. Renard[6]

[1]*Sorbonne Université, UPMC Université Paris 6; CNRS/INSU, LATMOS-IPSL; Université Versailles St-Quentin, 11 bld d'Alembert, F-78280 Guyancourt, France*
[2]*Sorbonne Université, UPMC Université Paris 6; CNRS/INSU; LATMOS-IPSL, 4 place Jussieu, F-75005 Paris, France*
[3]*Space Telescope Science Institute, Baltimore, MD 21218, USA*
[4]*Department of Physics, Assam University, Silchar 788011, India*
[5]*Université Paul Sabatier UPS; CNRS/INSU, IRAP/OMP, UMR 5277, 9 avenue Colonel Roche, F-31500, Toulouse, France*
[6]*LPC2E-CNRS, Université d'Orléans, 3A avenue de la recherche scientifique, F-45071 Orléans cedex 2, France*

Accepted 2017 January 5. Received 2016 December 16; in original form 2016 July 8

ABSTRACT

Remote observations of the light scattered by dust particles in comet 67P/Churyumov–Gerasimenko (67P/C-G) (photometry and imaging polarimetry) allow us to compare the deduced physical properties of these particles with *in situ* measurements provided by the *Rosetta* mission. Onboard experiments on the dust confirm properties inferred from polarimetric observations and from laboratory experiments, namely the existence of large dark particles in the size range 10–500 μm, which could be fluffy and compact aggregates of smaller grains (submicron- to micron-sized) and possibly of compact particles. The 2008–2009 apparition of comet 67P/C-G allowed us to observe the comet with two telescopes under a French–Indian collaboration. From the photometric and polarimetric observations, we inferred the presence of slow-moving, large compact particles in the coma before perihelion and eventually after. The additional ejection of fluffy aggregates of submicron-sized grains was consistent with observations after perihelion. In 2014–2015, as part of a worldwide campaign, observations of 67P/C-G were carried out in order to follow the evolution of the dust coma during the *Rosetta* mission. The campaign included observations with the *Hubble Space Telescope*, and photometric observations with the Himalayan Chandra Telescope in India. The comet was very active for about three months after perihelion, showing collimated jets, the structure of which changed over time, and a long dust tail. Using new published polarization values for observations in 2010, we were able to compare pre- and post-perihelion data and also to build partial phase curves for 67P/C-G (limited to phase angles smaller than 40°).

Key words: methods: observational – techniques: photometric – techniques: polarimetric – comets: general – comets: individual: 67P/Chruryumov–Gerasimenko.

1 INTRODUCTION

The properties of dust particle are usually deduced from the properties of the light that is scattered, including its linear polarization, infrared emissions and dynamics. For 67P/Churyumov–Gerasimenko (hereafter 67P/C-G), numerous remote observations were obtained during previous apparitions. However, because the comet is faint**,** some observational techniques were difficult to use. Previous *in situ* observations from *Rosetta* (OSIRIS, GIADA, COSIMA, MIDAS) (Rotundi et al. 2015; Hilchenbach et al. 2016; Bentley et al. 2016) provided a very good understanding of this comet's dust from the imaging of particles captured on targets onboard the spacecraft, with a resolution down to 10 μm with COSIMA (Langevin et al. 2016) and down to tens of nanometres with MIDAS (Mannel et al. 2016).

Captured interplanetary dust particles, collected in the Earth's stratosphere (with a size range up to 100 μm for aggregates and more compact particles), can be analysed in a laboratory. Ultra-carbonaceous micro-meteorites, collected in Antarctica in regions preserved from pollution and alteration, appear to be of cometary origin (Dobrica et al. 2012). In addition, some dust particles captured by *Stardust* directly from the coma of comet 81P/Wild

★ E-mail: edith.hadamcik@latmos.ipsl.fr (EH); Anny-Chantal.Levasseur-Regourd@latmos.ipsl.fr (ACL-R)

Table 1. Log of the observations in the red-wavelength domain. d = days (– before perihelion, + after perihelion), Δ Earth distance, Rh solar distance, mv = visual magnitude, α phase angle, PA position angle, Filters: CR, $\lambda = 684$ nm, $\Delta\lambda = 9$ nm; R, $\lambda = 650$ nm, $\Delta\lambda = 90$ nm; Rb, $\lambda = 630$ nm, $\Delta\lambda = 120$ nm. The 2.0-m IUCAA/Girawali telescope is located in India, and the 0.80-m OHP in France.

Date	Time to perihelion [d]	Δ [au]	R_h [au]	m_v JPL	α [°]	Sun–comet PA (°)	Filters
India, 2008							
Dec. 25	−65	1.67	1.45	14.2	35.8	70.5	CR
Dec. 26	−64	1.67	1.46	14.2	35.8	70.4	CR
Dec. 27	−63	1.67	1.46	14.2	35.8	70.3	CR & R_b
France, 2009							
March 17	+17	1.72	1.26	13.5 (12)	34.7	69.9	R
March 18	+18	1.73	1.27	13.5 (12)	34.7	70.0	R
March 19	+19	1.73	1.27	13.5 (12)	34.6	70.2	R
India, 2009							
April 30	+61	1.99	1.44	14.5	28.9	82.3	R_b
May 1	+62	2.00	1.45	14.5	28.7	82.7	R_b

2 have given clues on both compact particles and large aggregates with submicron- to micron-sized constituent grains. These particles have been analysed in many laboratories (e.g. Hörz et al. 2006; Burchell et al. 2008).

In situ observations of the dust in the inner coma of comet 67P/C-G by *Rosetta* provided a unique opportunity simultaneously to observe the scattered light and to collect and image particles very close to the nucleus (down to about 10 km) for the first time. Before perihelion, large aggregates (>100 μm) were observed on the COSIMA targets (Schulz et al. 2015). Later, a large variety (regarding structure and strength) of particle clusters, probably originating from the disruption of aggregates larger than 1 mm, were collected in the coma (Fulle et al. 2015). The 3D images obtained by MIDAS have revealed a hierarchical structure of particles, with submicron-sized subunits. They seemed to be dark (albedo in the range 0.01–0.1); some of them were porous aggregates with various structures; and others were more compact with irregular shapes (Schulz et al. 2015; Langevin et al. 2016; Bentley et al. 2016; Mannel et al. 2016). The elemental composition of the dust particles was heterogeneous: the particles could contain typical silicates such as olivine and pyroxenes as well as iron sulfides, which contribute to darkening the surface (Hilchenbach et al. 2016). Similar results on the sizes of the particles and their structures were obtained from an analysis of the scattered light measured by the OSIRIS camera and GIADA (Rotundi et al. 2015). Compact particles (80 to 800 μm) originate mainly from the active neck regions (Della Corte et al. 2015) but also from sporadic jets in the illuminated regions (Vincent et al. 2016). These compact particles account for about 15 per cent of the total number of particles detected by GIADA during the bound orbit of Rosetta, from 2014 September 15 to 2015 February 5 (Della Corte et al. 2015). Although it is difficult to know where the particles were ejected from, it may be that fluffy particles were found everywhere and that compact particles were more localized, including near perihelion when numerous jets were observed. However, at that time, *Rosetta* was relatively far from the nucleus (Della Corte et al. 2015).

We first summarize the 2008–2009 observations in order to allow a comparison with remote observations obtained in 2014–2015. We also present new observations: photometric observations obtained in 2015 November from the *Hubble Space Telescope* (*HST*), integrated polarization values for the same period, and photometric observations obtained in 2015 December from the Himalayan Chandra Telescope (HCT) in India. This enables us to compare the coma

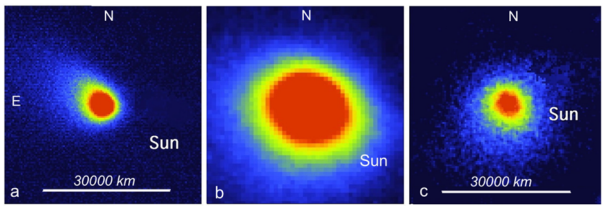

Figure 1. Typical intensity images for the three observational periods (in negative for the printed version). Field of view = 45 000 km. (a) 2008 December 27, 63 d before perihelion: asymmetric coma with a tailward feature. (b) 2009 March 18, 18 d after perihelion: coma elongated in the solar–antisolar direction. (c) 2009 May 1, 62 d after perihelion: coma nearly symmetric, faint features, if any. (Updated from Hadamcik et al. 2010.)

structures and to follow the evolution of the jets in the coma for about one month from 2015 November to December. Then, we compare the dust properties obtained from the remote observations by various techniques with observations of other Jupiter-family comets (JFCs) and their dust particle properties. Finally, we discuss the observational results in the light of laboratory results for transparent and dark particles as a function of their size and structure and the ground-truth provided by dust experiments onboard *Rosetta*.

2 SUMMARY OF REMOTE OBSERVATIONS IN 2008–2009

The main results, as obtained through a French–Indian collaboration at Observatoire de Haute-Provence (OHP, France) and at IUCAA Girawali Observatory (India) for three observational periods before and after perihelion (Hadamcik et al. 2010), have been re-analysed, taking into account the ground-truth provided by the *Rosetta* mission and remote observations in 2014–2015. The log of the observations can be found in Table 1.

2.1 Evolution of coma morphology

Before perihelion (−63 days), the coma was elongated tailwards (Fig. 1). Just after perihelion (+18 days), when the comet activity was high, the coma remained asymmetric and was elongated in a solar–antisolar direction (Figs 1 and 2). The main structures (jets and tail) are clearly seen in the rotational gradient-emphasized images

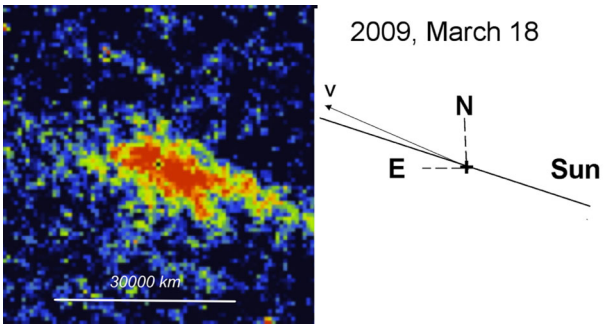

Figure 2. Emphasized intensity image for observations on 2009 March 18 (in negative for the printed version). Field of view = 80 000 km; north is up and east is to the left; V is the direction of motion of the comet. Jets are detected all around the photocentre (solar and anti-solar directions and south-west), and a linear structure is seen in the direction opposite to the movement (possible antitail).

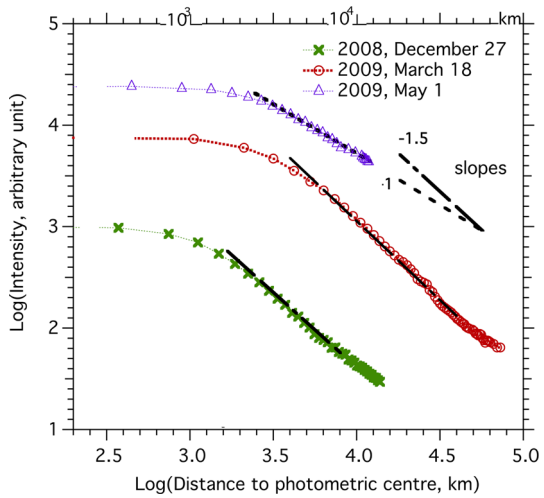

Figure 3. Azimuthally integrated radial profiles for the three observing periods on a log–log scale (with distances in kilometres on the upper horizontal axis). Linear fits identify changes in slope for the first two periods. Near the photocentre the slope is always low. (Updated from Hadamcik et al. 2010.)

(Larson & Sekanina 1984) about three weeks after perihelion, with an increase of activity seen for example in March 18 observations (Fig. 2). For more than two months after perihelion (+62 days), the coma seemed nearly symmetric. During that period, the comet was relatively faint ($m \geq 14$) and difficult to observe in polarization with narrowband continuum filters. The jets, if present in the coma, were undetectable.

2.2 Profiles of intensity through the coma

For each period, a profile with azimuthally integrated radial decrease is presented in Fig. 3. The linear fits out of the central regions indicate three main regions in the coma. Near the photocentre, the profiles are dominated by seeing, respectively, up to about 300 km for 2008 December, up to 1000 km for 2009 March, and up to 450 km for 2009 May. Farther away from the photocentre, the slopes are shallow (−0.7, −0.8) in the range 300–2000 km in December (about two months before perihelion), in the range 1000–4500 km in March (about three weeks after perihelion), and in the range 450–3500 km in May (about two months after perihelion). For increasing distances and the two first periods, the slope becomes steeper, reaching −1.5 up to 8500 km pre-perihelion and 60 000 km three weeks after perihelion. At larger distances and two months

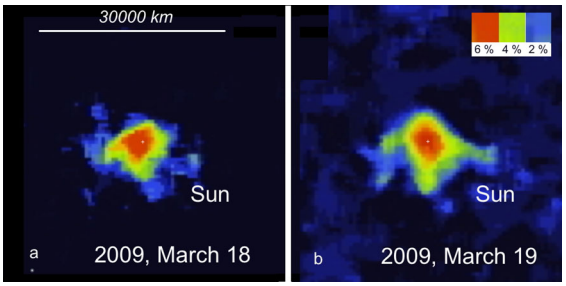

Figure 4. Polarization maps. Field of view = 45 000 km. (a) 2009 March 18, (b) 2009 March 19. All the structures have their origin at the centre. Same orientation as in Fig. 2, with north up, east to the left and the Sun in the south-west. The structures seem to extend from 18 to 19 March. (Updated from Hadamcik et al. 2010.)

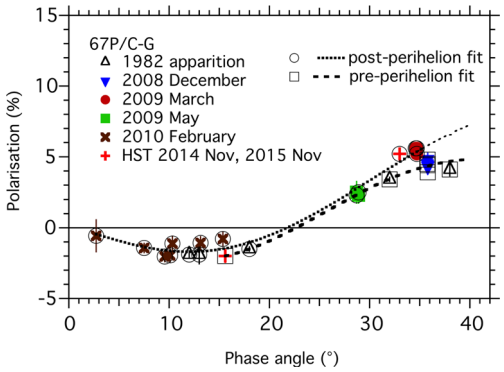

Figure 5 Linear polarization data as a function of phase angle for 67P/C-G. Data from Myers & Nordsieck 1984 (1982 observations); Hadamcik et al. 2010 (2008–2009 observations); Stinson et al. 2016 (2010 observations); Hines & Levasseur-Regourd 2016 (2014 observations); this work for *HST* in 2015 November at a 33° phase angle. A difference between the two phase curves, fitted for data before and after perihelion, is visible at least for phase angles above 30°. Some error bars are smaller than the signs. The errors are taken into account in the two fits. Red-wavelength domain.

after perihelion, the slope is close to the classical value of −1 corresponding to a homogeneous isotropic coma. The slope variations indicate a change in the average properties of the particles (e.g. in their size distribution, structure and/or complex refractive indices).

2.3 Linear polarization

2.3.1 Polarization maps

Polarization maps could be built for the period when the comet was most active (in 2009 March, two weeks after perihelion). The dust ejected near the photocentre was more polarized than the surrounding coma. In the 3000-km aperture the polarization was of the order of 6 per cent, while in the surrounding coma it was less than 2 per cent (Fig. 4). The polarization decreased with radial distance. As the particles from the jets moved away from the nucleus, they mixed with background particles with potentially different physical properties. Selection by size or some fragmentation may also occur: as the dust particles leave the inner coma, the largest particles could stay closer to the nucleus for a longer time.

2.3.2 Polarization phase curves

The polarization as a function of the phase angle is presented in Fig. 5 using all the available data up to 2015. Pre- and post-perihelion fits were derived from all available polarimetric

Table 2. Log of the observations for *HST* and HCT. – before perihelion, + after perihelion, Δ Earth distance, Rh solar distance, mv = visual magnitude, α phase angle, PA position angle.

Telescope and dates	Average time to perihelion	Δ [au]	R_h [au]	m_v, JPL	α [°]	Sun–comet PA [°]	Filter
HST 2014, Aug 18-19-20	−1 year	2.75	3.53	19.0	≈12	∼258°	596.6 nm, $\Delta\lambda = 234$ nm (F606W)
HST 2014, Nov 16-17-18	−9 months	3.43	2.96	19.4	≈16	∼264°	*idem* (F606W)
HST 2015, Nov 10-11-12	+ 3 months	1.80	1.63	15.0	≈33	∼115°	*idem* (F606W)
HCT 2015, Dec 12	+4 months	1.71	1.87		≈27	∼115°	600 nm, $\Delta\lambda = 140$ nm

data in the red domain. For phase angles smaller than 18°, the two fits are similar, although the lack of pre-perihelion data makes the comparison difficult. In contrast, a dichotomy can be noticed on the positive branch (in the 32°–40° phase angle range), with polarization higher after perihelion than before. This result may provide a clue to changes in the properties of dust particles ejected immediately after perihelion passage. The inversion angle is similar for the two fits: $\alpha_0 = 22° \pm 2°$; the slope at inversion is $h = (0.37 \pm 0.01)$ per cent per degree pre-perihelion and $h = (0.35 \pm 0.02)$ per cent per degree post-perihelion. The minimum polarization only measured post-perihelion is $P_{min} = (-1.7 \pm 0.1)$ per cent at the phase angle $\alpha_{min} = 12° \pm 3°$. The scatter of the data depends on the size of the aperture, on the heliocentric distance, or on seasonal effects resulting from the inclination of the rotation axis and the illumination of an irregularly shaped nucleus (Hadamcik et al. 2010; De Sanctis et al. 2010). Three weeks after perihelion the comet was quite active at a phase angle of about 34°–35°, and the polarization values are compatible with those measured by *HST* in 2015 November at a phase angle of 33° (see Section 3.1.3). At a phase angle of about 29°, two months after perihelion, in 2009 May, jet activity was difficult to detect, and the polarization values were smaller and below the phase curve corresponding to post-perihelion data. The seasonal effect caused by the asymmetry and obliquity of the nucleus (52°) was also observed by VIRTIS onboard *Rosetta* (Sierks et al. 2015; Tosi et al. 2015).

3 OBSERVATIONS IN 2014–2016

Two telescopes were used, namely the *HST* for photometry and imaging polarimetry, and the 2-m HCT in India for photometry. The log of the observations can be found in Table 2. – before perihelion, + after perihelion, Δ Earth distance, Rh solar distance, mv = visual magnitude, α phase angle, PA position angle.

3.1 *HST* observations

During the *Rosetta* mission, observations of 67P/C-G were possible with the *HST* using the Wide Field Camera (WFC) module of the Advanced Camera for Surveys (ACS) (Ford et al. 1998). A red filter (F606W) was used. Periods with particular interest for the *Rosetta* mission were chosen. Details of the observational techniques can be found in Hines et al. (2014). The results for observations before perihelion at phase angles of 12° and 15.°7 can be found in Hines & Levasseur-Regourd (2016).

The polarization integrated value on a 1200-km aperture around the photocentre was (-2 ± 0.5) per cent, which is similar to values previously found at such a phase angle by other observers (Fig. 5). A jet was visible at about 55° clockwise from the solar direction. Photometric results and integrated polarization values are presented here for 2015 November observations, about three months after perihelion.

3.1.1 *Coma morphology*

The comet was very active, with numerous jets (Fig. 6). An intensity image in log-scale shows the jets in the inner region of the coma in a field of view (FOV) of 6000 km (Fig. 6a). In Figs 6(b) and (c), showing the isophotes and rotational gradient image, the coma is asymmetric (FOV of about 120 000 km) and the tail is well developed. Four main jets distributed all around the photocentre are apparent. The longest jet, defined as jet 1, is at position angle (PA) ≈ 130°, jet 2 is at PA ≈ 180°, jet 3 is at PA ≈ 45°, and finally jet 4 (which seems to be close to jet 2 but is shorter) is at PA ≈ 207°. The angles are measured from north to east. The solar direction is at a PA of 115°, and the tail is in the antisolar direction with a PA of 295°. On the rotational gradient image, jet 2 is curved in the tail direction (owing to effect of the solar radiation pressure, also visible in Fig. 6b on the isophotes). Smaller jets, in the tail direction, in the first 500 km, are seen on the treated image. At larger radial distances, the tail consists of two regions. The inner part ends at about 10 000 km from the photocentre with an extension of about 60°. Farther away, the tail has an extension of about 20°.

3.1.2 *Intensity profiles as a function of the photocentric distance*

The intensity profiles are analysed as a function of the photocentric distance (Fig. 7). The azimuthally integrated radial decrease of intensity on a log–log scale has a shallow slope of −0.8 at less than 150 km; it is steep (−1.6) in the range 200–500 km; farther away, the slope is about −1 in the range 600–20 000 km. The decrease in intensity along the solar direction reveals four regions: (i) close to the photocentre, at less than 200 km, the slope is shallow (about −0.4); (ii) in the range 200–400 km, the slope is steep (about −1.4); (iii) farther away, in the range 400–10 000 km, the slope is about −1; (iv) finally, in the range 10 000–17 000 km, the slope is −1.35. The tailward profile also shows four regions: (i) closer than 200 km from the photocentre, the slope is shallow (about −0.45); (ii) in the range 200–1000 km, in the region with small jets, the slope is steep (−1.4); (iii) farther away (1000–10 000 km), a shallow slope of −0.86 is measured; (iv) finally, in the external region (10 000–31 000) km, the slope is −0.77.

In summary, the slope is shallow at distances smaller than about 150 km, and steepens (−1.4, −1.5) for photocentric distances in the range 200–400 km sunwards and 1000 km tailwards. Out of this region, the slope presents the classical value of −1, indicating a stable average outflow of dust. For the outer regions, the slope is again steep in the solar direction and shallow in the tail direction.

In the case of jet 1, the solar direction and the projected jet direction were very close to one another; the dust moved progressively back and replenished the tail at various photocentric distances. In the case of jet 2, the initial projected direction was at 66° from the solar direction, and this jet was curved towards the southern region of the image.

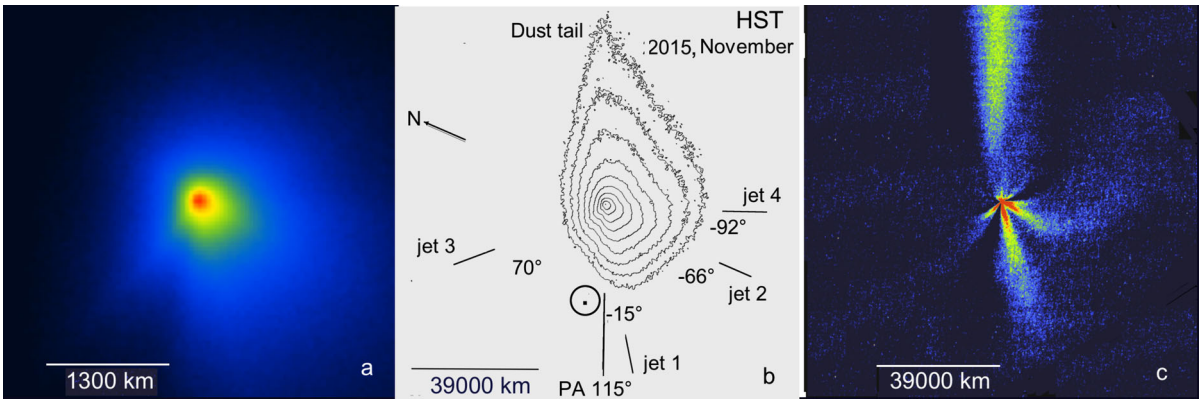

Figure 6. Intensity images for 2015 November 10–12, from *HST* observations (in negative for the printed version). The phase angle is about 33°. The solar direction is at the bottom of the images; PA is the position angle related to the north to east directions. (a) Inner coma on a log-scale for the intensity, field of view (FOV) = 6000 km. (b) Isophotes, indicating the overall coma structure and the main jet directions, FOV = 120 000 km. The position angle of the jets is related to the solar direction (positive when clockwise and negative when anticlockwise). (c) Treated intensity image emphasizing the structures, FOV = 120 000 km. Jet 2 appears clearly curved under the effect of radiation pressure; in Fig. 2(b), the more extended coma on the right side of the image (south) is due to this curved jet.

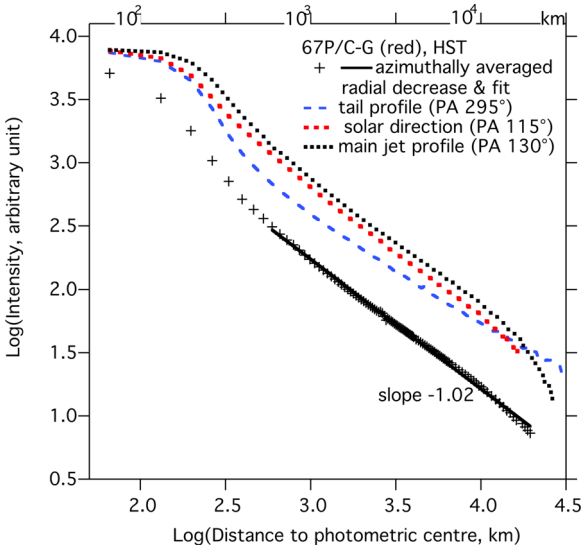

Figure 7. Comparison of the sunward, tailward and jet 1 profiles with the azimuthally integrated radial profile, on a log–log scale (with distances in kilometres on the upper horizontal axis). On the tailward profile, three regions can be noticed. The change in slope is evident at a photocentric distance of about 400 km. Jet 1 is close to the sunward direction; the two profiles are similar. The values are normalized at photocentre.

3.1.3 Aperture linear polarization

The polarization values (P) were measured in apertures centred on the photocentre: for a diameter of 18 000 km, $P = (5.2 \pm 0.5)$ per cent. For a smaller aperture of about 10 000 km, $P = (3.8 \pm 0.5)$ per cent. An analysis of the polarization observed from *HST* in the various regions will be detailed in Hines et al. (in preparation). The integrated polarization is compared with other observations in Fig. 5. Some weeks after perihelion, it was comparable to the 2009 values, confirming the change in the optical properties of dust ejected after perihelion (Section 2.3.2). It may also be noted that the polarization values in the different apertures seem to be qualitatively in agreement with the polarization map for observations obtained on 2015 November 8 using the SAO 6-m telescope (Snodgrass et al. 2016 and Section 4.1.2).

3.2 HCT observations

67P/C-G was observed in photometry on 2015 December 12 with the 2-m HCT in India. The comet–Earth distance of $\Delta = 1.71$ au made it possible to obtain observations of the relatively faint comet with good resolution. Details of the photometric observations can be found in Sen et al. (in preparation). Bessel red (600 nm, $\Delta\lambda$ 140 nm) and Bessel infrared (770 nm, $\Delta\lambda$ 170 nm) filters were used. Intensity images of the comet in the red domain are presented in Fig. 8. Four months after perihelion the comet was active, with numerous jets. The coma was asymmetric; the tail was well developed with a length of more than 80 000 km. The position angles of the main jets were measured on the isophotes and on the intensity image analysed by a rotational gradient method, as shown in Fig. 8. The longest jet, defined as jet 1, is at PA $\approx 135°$, jet 2 is at PA $\approx 200°$ and jet 3 is at PA $\approx 56°$. The solar direction is at PA $\approx 115°$ and the tail is at PA $\approx 300°$ (PA is related to the north to east directions). The overall shape of the coma agrees with the *HST* observations taken one month before. Compared with the solar direction, the main jets are close to the position angles measured for the *HST* observations; some smaller jets are less extended in projection on the sky, owing to changes in the projected coma structure with the change of the phase angle. In the Gemini enhanced images for 2015 November 1, December 6 and 2016 January 19 (Snodgrass et al. 2016), two jets are also observed close to the solar and south directions, in agreement with *HST* and HCT observations.

The radial decreases in intensity as a function of photocentric distance are presented in Fig. 9. Close to the photocentre, all the profiles follow a similar decrease with a shallow slope (this may be partially as a result of some seeing effect); a slope of -0.3 is found for the integrated profile and the sunward profile in the range 1000–2000 km; tailwards, in the range 1400–2600 km, the slope is -0.53. These shallow slopes could be caused by slowly moving large particles near the photocentre. The azimuthally integrated intensity slope is about -1 in the range 2200–21 000 km; in the sunward profile, this slope increases progressively up to -1 in the

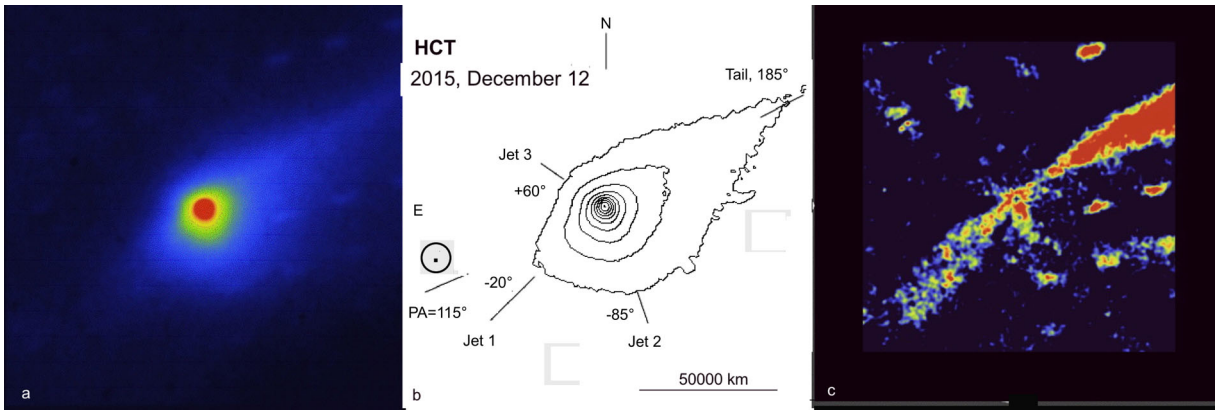

Figure 8. Intensity images for 2015 December 12, HCT observations (in negative for the printed version). The phase angle is 27°, and all the fields of view are 147 200 km. The solar direction is south-east, and PA is the position angle related to the north to east directions. (a) Image. (b) Isophotes showing the positions of the main jets. The position angles of the jets are related to the solar direction, to be compared with the *HST* results (positive when clockwise and negative when anticlockwise). (c) Rotational gradient-treated image to emphasize the main structures (star tracks are also shown, indicating the direction of motion of the comet).

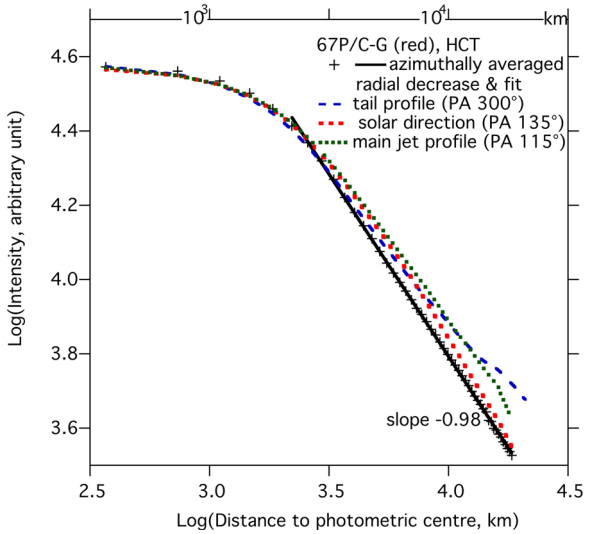

Figure 9. Comparison of the sunward, tailward and main jet profiles with the azimuthally integrated radial profile, on a log–log scale (with distances in kilometres on the upper horizontal axis). Compared with the *HST* observations in Fig. 7, the average profile is closer to the classical −1 slope. Close to the photocentre the sharp decreases are not detected (owing to the lower resolution of the telescope, seeing or variation of the dust properties). Tailwards, the slope decreases progressively, and sunwards it increases (position of jet 1).

range 5000–21 000 km. Jet 1 gradually takes up a direction of 20° from the solar direction. The particles moving in the jet are no longer observed sunwards. Tailwards, the slope is −0.79 in the range 2600–3700 km. Farther away, at 12 000–21 000 km, the slope decreases progressively to −0.58.

4 DISCUSSION

The dust environment of 67P/C-G, as revealed by experiments that studied dust particles onboard *Rosetta*, matches conclusions from ground-based observations regarding size distribution, change in brightness along the orbit, and whole-coma polarization (see e.g. Fulle et al. 2016; Snodgrass et al. 2016; Fig. 5 of the present paper).

4.1 67P/C-G particle properties from remote and *in situ* observations

4.1.1 Radial decrease of intensity and variation of particle size

The variation of slope on the radial intensity profiles as observed in 2009 March (three weeks after perihelion, when the brightness was at its maximum, in the photocentric distance range 4500–60 000 km) is similar to that found by Schleicher (2006) in 1996 January (one week after perihelion, in the photocentric distance range 2500–20 000 km), with a steep radial decrease of about −1.4. The behaviour of the intensity variations with a shallow slope close to the photocentre is interpreted to be caused by large slowly moving particles, which linger in the coma, and smaller dust particles farther away, where a sharp slope was found.

The shallow slope observed with *HST* in 2015 November (three months after perihelion) in the first 150 km may be the result of an significant concentration of large particles just after their ejection. The steep slope at distances in the range 200–500 km (or 1000 km tailwards) suggests the sporadic and rapid sublimation and fragmention of small particles. At large photocentric distances, in the solar direction, the particles were pushed tailwards by the solar radiation pressure, and the intensity profile steepened. Four months after perihelion, the sharp decrease is no longer detected on the radial profiles with HCT. The progressive change in the radial profiles with time to perihelion (with a decrease of the spatial extension of the steep slope) suggests a change in the dust properties, as indicated by the change in the mass differential power index (−2 beyond 2 au inbound, −3.7 at perihelion, and −4 at 2 au outbound), corresponding to smaller particle sizes and higher speeds by perihelion and for some time afterwards (Fulle et al. 2016; Della Corte et al. 2016).

4.1.2 High-polarization regions, and the size and structure of particles

After perihelion, on the polarization maps obtained in 2009 March (Fig. 4), the development of the jets in about 24 hr could suggest the presence of fast-moving micron- or submicron-sized grains, possibly as parts of quite fragile aggregates. However, the presence of slowly moving large dark compact particles cannot be excluded within 10 000 km from the nucleus, as suggested by the

shallow slope in the inner region and the sharp decrease at greater photocentric distances (see Figs 3 and 7). Large dark particles and fast-moving small grains, as suggested from observations obtained three weeks after perihelion, may have produced the high polarization (see Section 4.3, Fig 11). On the SAO polarimetric image obtained in 2015 November, three months after perihelion (Snodgrass et al. 2016), the polarization, which is high near the photocentre, decreases by 10 000 km, and increases again farther away, suggesting changes in the particle properties. The jets visible on intensity images are not obvious on the polarization map.

Jets imaged by *Rosetta* cameras are difficult to relate to the jet-like features detected from Earth, which could be the result of numerous small-scale jets originating from the nucleus (Lara et al. 2015). Particles ejected from the nucleus are more or less compact aggregates of aggregated grains that may fragment (Bentley et al. 2016; Mannel et al. 2016). The fluffy particles could originate from the whole surface (Della Corte et al. 2015).

4.2 Comparison with other comets

A comparison using not only polarimetry (high- and low-polarization comets) but also dust-to-gas production rates and strengths of the silicate emission bands in mid-infrared spectroscopy may be used to classify comets in relation to their dust particle properties (Hanner 2003). For comets with a low maximum in polarization, the strength of silicate emission bands in the mid-infrared is low. Conversely, a strong correlation is found between high-polarization comets and strong silicate features, these comets being usually dust-rich (e.g. Levasseur-Regourd, Hadamcik & Renard 1996; Kolokolova et al. 2007). This correlation has been suggested to come from submicron-sized grains in fluffy aggregates, and from the presence of dark organics allowing the thermal excess (Hanner 2003). However, JFCs are seldom observed at large phase angles, making it difficult to obtain a classification by polarimetric phase curves.

67P/C-G is dust-rich (Hanner et al. 1985; Rotundi et al. 2015). Interestingly, numerous polarimetric observations of 67P/C-G have established (see Fig. 5) that a comet may have different polarimetric behaviours before and after perihelion. No emission band was found close to perihelion, and Hanner et al. (1985) suggested the presence of large relatively compact particles. These authors nevertheless suggested the presence of dark grains smaller than 10 μm from a temperature higher than expected for a blackbody. These apparently contradictory suggestions correspond to increases in polarization and in the power-law index of the differential size distribution (Fulle et al. 2016), correlated with the emission of small grains together with highly porous particles (Hage & Greenberg 1990; Kelley & Wooden 2009). It is now understood that part of the southern hemisphere is illuminated only soon before perihelion and that its surface becomes rapidly and briefly warm at each perihelion return (Sierks et al. 2015; Della Corte et al. 2016).

Comet 81P/Wild 2, another JFC, was also dust-rich (A'Hearn et al. 1995; Fink, Hicks & Fevig 1999). A polarization of about 5 per cent was measured at phase angles of about 37° (Hadamcik & Levasseur-Regourd 2003), which is close to values measured for the low-polarization class and for 67P/C-G before perihelion (Fig. 5), and of about −2 per cent at a phase angle of 10°. A broad, shallow silicate feature was found (Hanner & Hayward 2003) without any difference before and after perihelion. The *Stardust* mission revealed variations in flux over small spatial scales, suggesting the presence of fluffy aggregates at various locations within the coma (Tuzzolino 2004; Levasseur-Regourd 2004). The *Stardust* samples revealed both compact particles and submicron-sized grains in aggregates (e.g. Hörz et al. 2006). The presence of fluffy particles was confirmed in the coma of 67P/C-G (e.g. Schulz et al. 2015; Bentley et al. 2016; Kolokolova 2016). As for 67P/C-G, a smaller positive-polarization region was observed around the centre, which was the case for 67P/C-G, three months after perihelion. For 81P/Wild 2, a very negative polarization was also observed around the photocentre at small phase angles (Hadamcik & Levasseur-Regourd 2003). 67P/C-G was compared with other specific comets (a discussion of which is outwith the scope of the present paper): it seemed to be a classical JFC from its dust properties (Hadamcik & Levasseur-Regourd 2009; Hadamcik et al. 2010). Its peculiar seasonal effect is probably induced by its shape.

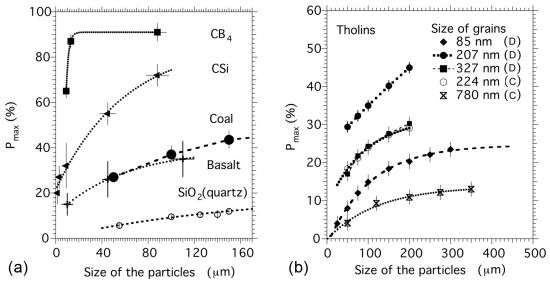

Figure 10. Polarization value versus size of the particles. (a) Compact particles with increasing absorption from bottom to top. (b) Aggregates of two organic materials with different absorption and size of the constituent grains [(D) is dark brown, (C) is clear]. (Updated from Hadamcik et al. 2009.)

4.3 Interpretation of observations from experimental simulations

In order to interpret the light-scattering and polarization observations, experimental simulations (together with numerical ones, limited to particles with sizes below 10 μm) were carried out. The *Rosetta* results have already established a wide distribution of sizes of dust particles. The light scattered by free-floating particles in an optically thin cloud has been studied using the PROGRA^2 instruments (e.g. Hadamcik et al. 2011; Levasseur-Regourd et al. 2015). The scattered light mostly depends on the size (and size distribution) of the particles and of their constituent grains, on their structure and morphology, and on their complex refractive indices (related to their composition and their albedo). Systematic results for the influence of the sizes (grains and particles) on the positive polarization (P), at phase angles larger than 25°, are illustrated in Fig. 10 by the variations of the maximum in polarization (P_{max}).

Fig. 10(a) is for compact particles of different absorptions, and Fig. 10(b) is for fluffy aggregates of submicron-sized grains for two organic materials, so-called tholins, one being dark brown (D), and the other one, with refractive indices close to those of silicates, being clear (C). For compact and fluffy particles, P_{max} values increase with the size of the irregular particles up to a maximum depending on the absorption. P_{max} increases when the size of the submicron constituent grains decreases in the aggregates.

In Fig. 11, P_{max} is compared for transparent silica samples and carbon samples. All particles have irregular shapes. The high-porosity (more than 80 per cent) aggregates are made up of a large number of constituent submicron-sized grains. The horizontal axis represents the size-parameter 'X' (ratio of the particle boundary size to the wavelength). P_{max} decreases when the size of the small

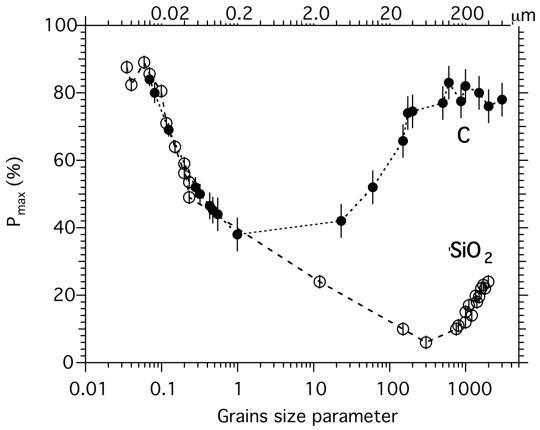

Figure 11. Polarization value versus size parameter X of the grains ($X = 2\,\mu s/\lambda$, where s is the equivalent radius and λ is the wavelength of meaurements). C, carbon black ; SiO_2, silica. (Updated from Hadamcik et al. 2009.)

grains increases, up to about 0.2 μm (size parameter of about 1) for absorbing carbon grains and up to about 24 μm for transparent silica. Similar high polarization values are found for black compact particles and fluffy aggregates of submicron-sized grains (Hadamcik et al. 2009). This finding was used to interpret the polarization regions in 67P/C-G at maximum activity (Section 4.1.2).

In order to ascertain which particles are responsible for the high polarization (e.g. near the nucleus or within the jets), other diagnostics are necessary in addition to the polarization values (e.g. the velocity of the particles). The evolution or variations of polarization in the coma may be interpreted in terms of the evolution of sizes and/or albedo, giving some insight into the refractive indices of the materials (Hadamcik et al. 2013). The difference in polarization values in the negative branch between comets is usually very small, in the (-1 ± 1) per cent range, but it can reach values of (-6 ± 1) per cent in the inner region of the so-called 'polarimetric halo' for some comets, for example 81P/Wild 2 (Hadamcik & Levasseur-Regourd 2003; Cochran et al. 2015). However, trends deduced experimentally for phase angles smaller than 20° are outwith the scope of this paper, which considers mainly differences in the positive branch.

To summarize, experimental and numerical simulations can provide interpretations of the variation (including evolution) in polarization in a cometary coma in terms of the sizes and refractive indices of the particles and grains (Hadamcik et al. 2011; Kolokolova et al. 2007; Lasue et al. 2009; Zubko et al. 2012). Experimental simulations allow the use of particles (aggregates and compact particles) with large size distributions up to 500 μm, including mixtures of tentatively realistic particles.

5 CONCLUSIONS

Using results from *Rosetta*, both the long-term evolution and short-term variations have been identified in the physical properties of dust particles released in the coma of 67P/C-G. Variations in intensity and polarization (e.g. jets) have been identified through past and present remote observations of 67P/C-G. Polarization values in the coma and their variations give clues as to the properties of the particles. *Rosetta* studies now give a ground-truth (e.g. the presence of very large compact or aggregated particles and their variations when the comet approached the Sun), providing a unique link to estimating some dust properties of a given comet, 67P/C-G, through polarimetry, in the likely absence of another rendezvous mission in the near future.

By combining observation techniques and results from simulations, it has been shown that, for most comets with high dust activity, small submicron-sized grains in fluffy aggregates are present in the jets and induce a high polarization. Their presence in 67P/C-G was not evident before *Rosetta*. Both kinds of particles can be found in a single comet, as demonstrated by *in situ* observations of 67P/C-G. The particles may be related to some specific structures such as large compact particles (or compact aggregates), which are more efficiently ejected by strong and sporadic jets, while small grains or large porous aggregates thereof are homogeneously spread out everywhere in the coma. The particles ejected are different before and after perihelion, as indicated by changes in the properties of the coma.

ACKNOWLEDGEMENTS

We thank Daniel Bardin for his help with the Observatoire de Haute Provence (OHP, France) observations; OHP, IUCAA Observatory (India) and Chandra Himalayan telescope (India) for attribution of observing time; and Programme National de Planétologie (PNP, France) for support. This work was partly supported by CNES, in relation to observations of MIDAS on the *Rosetta* mission and to measurements with PROGRA2 instruments on parabolic flights on A300-ZeroG. Support for *HST* comet observations in program numbers GO13863 and 144261 was provided by NASA through a grant from the Space Telescope Science Institute, which is operated by the Association of Universities for Research in Astronomy Incorporated, under NAS5-26555.

REFERENCES

A'Hearn M. F., Millis R. L., Schleicher D. G., Osip D. J., Birch P. V., 1995, Icarus, 118, 223
Bentley M. S. et al. 2016, Nature, 537, 73
Burchell M. J., Foster N. J., Kearsley A. T., Creighton J. A., 2008, MPS, 43, 135
Cochran A. L. et al., 2015, Space Sci. Rev., 197, 9
Della Corte V. et al., 2015, A&A, 583, A13
Della Corte V. et al., 2016, MNRAS, 462, S210
De Sanctis M. C., Lasue J., Capria M. T., Magni G., Turrini D., Coradini A., 2010, Icarus, 247, 341
Dobrica E., Engrand C., Leroux H., Rouzaud J.-N., Duprat J., 2012, Geochim. Cosmochim. Acta, 76, 68
Fink U., Hicks M. P., Fevig R. A., 1999, Icarus, 141, 331
Ford H. C. et al., 1998, SPIE 3356, Space Telescopes and Instruments, 234
Fulle M. et al., 2015, ApJ, 802, L12
Fulle M. et al., 2016, ApJ, 821, 19
Hadamcik E., Levasseur-Regourd A. C., 2003, J. Quant. Spectrosc. Radiat. Transfer, 79-80, 661
Hadamcik E., Levasseur-Regourd A. C., 2009, Planet. Space Sci., 57, 1118
Hadamcik E., Renard J.-B., Levasseur-Regourd A. C., Lasue J., Alcouffe G., Francis M., 2009, J. Quant. Spectrosc. Radiat. Transfer, 110, 1755
Hadamcik E., Sen A. K., Levasseur-Regourd A. C., Gupta R., Lasue J., 2010, A&A, 517, A86
Hadamcik E., Renard J.-B., Levasseur-Regourd A. C., Lasue J., 2011, in Mishchenko M. et al., eds, NATO Science for Peace and Security Program. Springer, Dordrecht, p. 137
Hadamcik E., Renard J.-B., Mahjoub A., Gautier T., Carrasco N., Cernogora G., 2013, Earth Planets Space, 58, 1175
Hage J. I., Greenberg J. M., 1990, ApJ, 361, 251
Hanner M. S., 2003, J. Quant. Spectrosc. Radiat. Transfer, 79–80, 695
Hanner M. S., Hayward T., 2003, Icarus, 161, 164

Hanner M. S. et al. 1985, Icarus, 64, 11
Hilchenbach M. et al. 2016, ApJ, 816, L32
Hines D. C., Levasseur-Regourd A. C., 2016, Planet. Space Sci., 123, 41
Hines D. C. et al., 2014, ApJ, 780, L32
Hörz F. et al., 2006, Science, 314, 1716
Kelley M. S., Wooden D. H., 2009, Planet. Space Sci., 57, 1133
Kolokolova L., 2016, Nature, 537, 37
Kolokolova L., Kimura H., Kisekev N., Rosenbush V., 2007, A&A, 463, 1189
Langevin Y. et al., 2016, Icarus, 271, 76
Lara L. M. et al., 2015, A&A, 583, A9
Larson S. M., Sekanina Z., 1984, AJ, 89, 571
Lasue J., Levasseur-Regourd A. C., Hadamcik E., Alcouffe G., 2009, Icarus, 199, 129
Levasseur-Regourd A. C., 2004, Science, 304, 1762
Levasseur-Regourd A. C., Hadamcik E., Renard J.-B., 1996, A&A, 313, 327
Levasseur-Regourd A. C., Shkuratov Y., Renard J.-B., Hadamcik E., 2015, in Kolokolova L., Hough J., Levasseur-Regourd A. C., eds, Polarimetry of Stars and Planetary Systems. Cambridge Univ. Press, Cambridge, p. 62
Mannel T. et al., 2016, MNRAS, 462, S304
Myers R. V., Nordsieck K. H., 1984, Icarus, 58, 431
Rotundi A. et al., 2015, Science, 347, 3905
Schleicher D. G., 2006, Icarus, 181, 442
Schulz R. et al., 2015, Nature, 518, 216
Sierks H. et al., 2015, Science, 347, 1044
Snodgrass C. et al., 2016, Phil. Trans. Roy. Soc., in press
Stinson A., Bagnulo S., Tozzi G. P., Boehnhardt H., Protopapa S., Kolokolova L., Muinonen K., Jones G. H., 2016, A&A, 594, 110
Tosi F. et al. 2015, EPSC2015-268, Nantes
Tuzzolino A. J., 2004, Science, 304, 1764
Vincent J.-B. et al., 2016, A&A, 587, 14
Zubko E., Muinonen K., Shkuratov Y., Hadamcik E., Levasseur-Regourd A. C., Videen G., 2012, A&A, 544, L8

This paper has been typeset from a TEX/LATEX file prepared by the author.